Maintenance Mechanism for the Teleconnection Pattern over the High Latitudes of the Eurasian Continent in Summer

Xinyu Li[*1], Riyu Lu[2, 3], Richard J. Greatbatch[4, 5], Gen Li[1], and Xiaowei Hong[3, 6]

[1]College of Oceanography, Hohai University, Nanjing 210098, China.

[2] State Key Laboratory of Numerical Modeling for Atmospheric Sciences and Geophysical Fluid Dynamics, Institute of Atmospheric Physics, Chinese Academy of Sciences, Beijing 100029, China.

[3] College of Earth and Planetary Sciences, University of the Chinese Academy of Sciences, Beijing 100049, China.

[4]Ocean Circulation and Climate Dynamics, GEOMAR Helmholtz Centre for Ocean Research Kiel, Kiel 24105, Germany.

[5]Faculty of Mathematics and Natural Sciences, University of Kiel, Kiel 24105, Germany.

[6] Climate Change Research Center and Nansen-Zhu International Research Centre, Institute of Atmospheric Physics, Chinese Academy of Sciences, Beijing 100029, China.

Submitted to *J. Climate*

May 20, 2019

Revised September 6, 2019

Revised October 21, 2019

Corresponding author:

Dr. Xinyu Li, E-mail: lixinyu@hhu.edu.cn

Early Online Release: This preliminary version has been accepted for publication in *Journal of Climate*, may be fully cited, and has been assigned DOI 10.1175/JCLI-D-19-0362.1. The final typeset copyedited article will replace the EOR at the above DOI when it is published.

ABSTRACT

There is a zonally oriented teleconnection pattern over the high-latitude Eurasian continent, which is maintained through baroclinic energy conversion. In this study, we investigate the unique features of the maintenance mechanism of this teleconnection. It is found that the baroclinic energy conversion is most efficient in both the mid-troposphere and the lower troposphere, and that the baroclinic energy conversion in the lower troposphere is comparable to that in the mid-troposphere. Further results indicate that the basic state plays a crucial role in the baroclinic energy conversion. For both the mid and lower troposphere, the atmospheric stability is low and the Coriolis parameter is large over high-latitude Eurasia, favoring strong baroclinic energy conversion. Particularly, in the lower troposphere, the atmospheric stability exhibits a clear land-sea contrast, favoring baroclinic energy conversion over the continents rather than the oceans. Furthermore, in the lower troposphere, the in-phase configuration of the meridional wind and temperature anomalies, which results from the strong meridional gradient of mean temperature around the north edge of the Eurasian continent, also significantly contributes to baroclinic energy conversion. This study highlights the role of the basic state of temperature rather than zonal wind in maintaining the high-latitude teleconnection through baroclinic energy conversion.

Accepted for publication in *Journal of Climate*. DOI 10.1175/JCLI-D-19-0362.1.

1 Introduction

Summer climate variability over the Eurasian continent is greatly affected by atmospheric teleconnection patterns or Rossby waves (e.g., Lu et al. 2002; Wu 2002; Ding and Wang 2005; Folland et al. 2009; Bladé et al. 2012; Ding et al. 2011; Hong et al. 2018; Li and Ruan 2018; P. Xu et al. 2019). Various teleconnection patterns have been used to explain regional anomalous rainfall (Wang 1992; Iwao and Takahashi 2006, 2008; Chen and Huang 2012; Sun and Wang 2012; Lin 2014; Li and Lu 2017; Lin et al. 2017a; Li and Lu 2018; Wang et al. 2018), temperature (Greatbatch and Rong 2006; Hong et al. 2017), and extreme events (Cassou et al. 2005; Wulff et al. 2017, K. Xu et al. 2019). Therefore, understanding the mechanisms responsible for these teleconnections is of scientific significance and has important implications for the prediction of weather and climate over Eurasia.

Many teleconnection patterns or Rossby waves in summer appear over a wide range of latitudes over the Eurasian continent, and thus can act as a dynamical link between the tropics and extratropics. Some of these teleconnections can be excited by tropical forcing and propagate poleward (e.g., Hoskins and Karoly 1981; Nitta 1987; Huang and Sun 1992; Wulff et al. 2017). Some examples are: (i) the well-known Pacific–Japan pattern (Nitta 1987) or East Asian–Pacific pattern (Huang and Sun 1992), which is associated with the anomalous convection over the tropical western North Pacific (Nitta 1986, 1987; Lu and Dong 2001; Lu 2004; Kosaka et al. 2011) and (ii) the Summer East Atlantic mode introduced by Wulff et al. (2017), which can be forced by diabatic heating anomalies of opposing signs in the tropical Pacific and Caribbean. On the other hand, some circulation modes exist without clear tropical forcing, such as the summer North Atlantic Oscillation (Feldstein 2007; Folland et al. 2009)

Accepted for publication in *Journal of Climate*. DOI 10.1175/JCLI-D-19-0362.1.

63 and the Eurasian pattern during summer (Yang 1992; Yang and Huang 1992; Lee et al. 2005;
64 Yoon and Yeh 2010).

65 Another kind of teleconnection pattern is confined to a limited range of latitudes over
66 the Eurasian continent during summer. The so called “Silk Road pattern” (SRP) is such a kind
67 of teleconnection (Lu et al. 2002; Enomoto et al. 2003; Yasui and Watanabe 2010; Chen and
68 Huang 2012; Hong and Lu 2016; Zhou et al. 2019). The SRP propagates zonally in the
69 mid-latitudes across the Eurasian continent along the upper-tropospheric Asian westerly jet,
70 which acts as a waveguide and confines the waves within it (Hoskins and Ambrizzi 1993;
71 Ambrizzi et al. 1995; Branstator and Teng 2017). The maintenance mechanism of the SRP
72 can be explained by the interaction between stationary waves and the basic flow (Sato and
73 Takahashi 2006; Kosaka et al. 2009; Yasui and Watanabe 2010; Song et al. 2013). The
74 perturbations associated with the SRP can efficiently extract kinetic energy from the basic
75 flow through barotropic energy conversion and available potential energy through baroclinic
76 energy conversion. Another important, but secondary, factor affecting the SRP is tropical
77 heating anomalies, for instance, rainfall anomalies associated with the Indian summer
78 monsoon (Ding and Wang 2005; Sato and Takahashi 2006; Ding et al. 2011; Chen and Huang
79 2012; Greatbatch et al. 2013).

80 Teleconnections or Rossby waves also appear at high latitudes over the Eurasian
81 continent in summer, as shown in previous studies, which focused on climate anomalies over
82 various regions and investigated the circulation anomalies responsible for the climate
83 anomalies (Wakabayashi and Kawamura 2004; Fukutomi et al. 2004; Iwao and Takahashi
84 2006, 2008; Lin 2014; Lin et al. 2017b). For example, Fukutomi et al. (2004) identified an

Accepted for publication in *Journal of Climate*. DOI 10.1175/JCLI-D-19-0362.1.

85 out-of-phase relationship in precipitation between eastern and western Siberia, and indicated
86 that this out-of-phase relationship is the result of stationary waves over northern Eurasia.
87 Nakamura and Fukamachi (2004) found that abnormal coolness over eastern Japan is greatly
88 affected by the Okhotsk high, and the Okhotsk high can be attributed to a stationary Rossby
89 wave that originates from northern Europe and extends to the Far East. Among the four
90 relevant teleconnection patterns responsible for anomalous summer climate in Japan
91 extracted by Wakabayashi and Kawamura (2004), two appear over northern Eurasia. Iwao
92 and Takahashi (2006) identified a north–south seesaw pattern in July precipitation between
93 northeast Asia and Siberia, and found that this seesaw pattern is associated with circulation
94 anomalies over northern Eurasia as well as those along the upper-tropospheric mid-latitude
95 westerly jet. These studies demonstrated that the teleconnections exist in the high latitudes
96 over the Eurasian continent and play an important role in affecting regional climate in
97 summer.

98 Recent studies presented more evidences of teleconnection patterns in the high latitudes
99 of the Eurasian continent. The Summer East Atlantic mode identified by Wulff et al. (2017) is
100 a teleconnection pattern that appears over the North Pacific, North America, North Atlantic
101 and the high-latitude west Eurasian continent. Wulff et al. (2017) suggested that this mode
102 can be forced by diabatic heating anomalies in the tropics. Li and Ruan (2018) introduced a
103 teleconnection pattern over the North Atlantic and the high latitudes of the Eurasian continent,
104 and explained this teleconnection pattern in terms of stationary Rossby waves originating
105 over the subtropical North Atlantic. These teleconnections include significant circulation
106 anomalies over the high latitude Eurasian continent, but they appear over a wide range of

Accepted for publication in *Journal of Climate*. DOI 10.1175/JCLI-D-19-0362.1.

latitudes, and are attributed to tropical or subtropical forcings. By contrast, P. Xu et al. (2019) reported a zonally-oriented teleconnection pattern propagating from the British Isles over the high-latitude Eurasian continent, and indicated that this teleconnection pattern shows only a loose relationship to external forcing. They suggested that this teleconnection pattern can be maintained through baroclinic energy conversion from the basic flow, while the barotropic energy conversion is much less efficient.

The present study aims to dig further into the physical mechanism for the occurrence and maintenance of the high-latitude teleconnection pattern over the Eurasian continent. We focus on the role of the basic state, rather than tropical and subtropical forcings. Actually, as a kind of basic states, the basic flow is very weak over the high-latitude Eurasian continent, and thus exhibits only weak shear both horizontally and vertically. This is in a sharp contrast to the mid-latitude Eurasian continent, where the basic flow exhibits a strong shear both horizontally and vertically, corresponding to the strong Asian westerly jet in the upper troposphere. One can attribute weak barotropic energy conversion suggested by P. Xu et al. (2019) to the weak horizontal shear of basic flows in the high-latitude Eurasian continent. However, how does the weak vertical shear of the basic flow induce the baroclinic energy conversion, which efficiently maintains the high-latitude teleconnection over the Eurasian continent? What are the unique features of the basic state favoring the occurrence and maintenance of the teleconnection over the high latitudes of the Eurasian continent? In this study, we make an exploration on these issues.

The rest of this paper is arranged as follows. Section 2 describes the data and methods. Section 3 presents the features of high-latitude Eurasian teleconnection pattern and the

Accepted for publication in *Journal of Climate*. DOI 10.1175/JCLI-D-19-0362.1.

associated baroclinic energy conversion. The results in this section indicate that the teleconnection pattern can effectively extract available potential energy from the basic flow in both the mid and lower troposphere. Therefore, Section 4 further illustrates the baroclinic energy conversion in the mid and lower troposphere, respectively. Section 5 is devoted to a summary and discussion.

2 Dataset and methods

The primary dataset used in this study is the monthly ERA-Interim dataset (Dee et al. 2011), on a horizontal resolution of 1.5°×1.5°. The analyzed time span is selected from 1979 to 2017. We also employed the National Centers for Environmental Prediction (NCEP)/National Center for Atmospheric Research (NCAR) reanalysis dataset (Kalnay et al. 1996) and the Japanese 55-year Reanalysis (JRA-55) dataset (Kobayashi et al. 2015) to repeat the main analyses and obtained similar results. In this study, we focus on the summer mean, which refers to the averages over June–August (JJA).

The main statistical methods used in the present study are empirical orthogonal function (EOF) analysis, regression analysis and correlation analysis. The method proposed by North et al. (1982) is used to test the statistical significance in the EOF analysis, and the Student's *t* test is used to determine the statistical significance in the analyzed results.

3 The high-latitude Eurasian teleconnection pattern and the associated baroclinic energy conversion

Figure 1 shows the climatological JJA-mean horizontal winds at 250 hPa. Here, we use 250 hPa to represent the upper troposphere rather than 200 hPa, considering that the thickness

Accepted for publication in *Journal of Climate*. DOI 10.1175/JCLI-D-19-0362.1.

of troposphere in the high latitudes is thinner than that in the mid-latitudes. The basic flow in the high latitudes shows distinctly different features from that in the mid-latitudes. For the zonal winds (Fig. 1a), the westerly jet stream spans across the North Atlantic and the mid-latitude Eurasian continent , with strong meridional shear to the north and south of the jet axis. Here, the jet axis is determined as the first derivative of zonal winds being zero. Over the high-latitude Eurasian continent, however, the zonal wind shows much more uniform features, with very weak zonal and meridional gradients. For the meridional winds (Fig. 1b), the mid-latitudes are characterized by alternatively southerly and northerly flows, with maximum amplitudes along the Asian westerly jet. Over the high-latitude Eurasian continent, by contrast, the meridional winds are weak. However, the meridional winds show strong standard deviations, indicating that the upper-tropospheric meridional winds over the region exhibit large interannual variability. The standard deviations are much stronger in the high latitudes than the mid-latitudes. It is notable that the cells of large interannual variability at the high latitudes are not corresponding to the cells of the climatological strong northerlies or southerlies.

Figure 2 shows the leading mode of 250-hPa JJA-mean meridional winds obtained by EOF analysis within the domain 55º−70°N, 35º−110°E, where the standard deviations of meridional winds are basically larger than 3.50 m s^{-1} (Fig. 1b). Prior to EOF analysis, the raw data are weighted by the square root of the cosine of latitude to obtain equal weight to equal areas. The leading mode explains nearly half of the total interannual variance of meridional winds (49.3%) and is significantly distinguished from the higher modes according to North et al. (1982). The analysis domain is deliberately separated from those used for the SRP

Accepted for publication in *Journal of Climate*. DOI 10.1175/JCLI-D-19-0362.1.

analyses over mid-latitudes conducted by previous authors (e.g., Yasui and Watanabe 2010; Hong and Lu 2016). The domain is also smaller than those used specially for high-latitude wave trains by previous authors (Xie and Kosaka 2016; P. Xu et al. 2019), since we attempt to highlight the main body of the wave train. In fact, the present results are not sensitive to the precise choice of EOF domain. As discussed in later analyses, the wave train can most effectively extract available potential energy from the basic flow for its growth and maintenance within the chosen analysis domain. In addition, we also conducted EOF analyses on the meridional wind and geopotential height at other levels, such as the geopotential height at 500 hPa or the meridional wind at 925 hPa, and obtained very similar wave trains and principal components (not shown). This is associated with the equivalent barotropic structure of the teleconnection pattern (P. Xu et al. 2019).

The leading mode is associated with a west–east seesaw pattern. In the positive phase, positive anomalies appear to the west of 67.5°E and negative ones to the east of this longitude, with the positive and negative centers near 46.5°E, 63°N and 90°E, 60°N, respectively. The correlation coefficient of JJA-mean 250-hPa meridional wind between these two centers is −0.63, consistent with the seesaw pattern of EOF1. These anomalies correspond well to the cells of strong standard deviations shown in Fig. 1b, suggesting that the leading mode significantly contributes to the total variance of interannual variability in the upper-tropospheric meridional winds.

In this study, we abbreviate the high-latitude Eurasian teleconnection to HET, and define a HET index (HETI) as the standardized difference in JJA-mean 250-hPa meridional winds between the two centers of EOF1, i.e., 46.5°E, 63°N minus 90°E, 60°N, to quantitatively

Accepted for publication in *Journal of Climate*. DOI 10.1175/JCLI-D-19-0362.1.

194 estimate the interannual variation of the HET. Therefore, the spatial pattern shown in Fig. 2a
195 is considered to be the positive phase of the HET. The HETI is shown as the red line in Fig.
196 2b. The HETI is highly correlated with PC1, with the correlation coefficient being 0.98.
197 Despite the high correlation, we prefer to use the HETI considering its simplicity. The HETI,
198 as well as PC1, exhibits clear interannual variation, but no distinct decadal variation.

199 Figure 3 shows the 250-hPa meridional wind anomalies regressed against the
200 normalized HETI. A clear teleconnection pattern appears over the high-latitude Eurasian
201 continent along 63°N, with alternatively southerly and northerly anomalies. The horizontal
202 wave activity flux (Takaya and Nakamura 2001) indicates that the HET is a stationary Rossby
203 wave train that originates from the North Atlantic and Europe and extends eastward across
204 the Eurasian continent. The teleconnection pattern is in good agreement with those shown by
205 previous studies (Xie and Kosaka 2016; P. Xu et al. 2019), and resembles the pattern of
206 500-hPa geopotential height identified by Li and Ruan (2018), particularly over the northwest
207 part of the Eurasian continent. The correlation coefficients between the HETI and the wave
208 train indexes defined by Li and Ruan (2018) and P. Xu et al. (2019) are −0.60 and 0.96,
209 respectively. On the other hand, to test the connection between the HET and the mid-latitude
210 SRP, the SRP index (SRPI) defined by Yasui and Watanabe (2010) is employed, which is
211 given by the standardized PC1 of EOF analysis on 200-hPa meridional winds over 20º−60°N,
212 0º−150°E. The correlation coefficient between the HETI and SRPI is only 0.10, suggesting
213 that these two teleconnection patterns are largely independent of each other.

214 In the following, we make a detailed inspection of the maintenance mechanism of the
215 HET using the analysis procedure adopted by Kosaka et al. (2009). We focus on the

Accepted for publication in *Journal of Climate*. DOI 10.1175/JCLI-D-19-0362.1.

baroclinic energy conversion (*CP*) associated with the HET. The barotropic energy conversion (*CK*) is not discussed here, as it is much less efficient in energy conversion (not shown), consistent with P. Xu et al. (2019). The evaluation of *CP* is based on the following formula (e.g., Kosaka and Nakamura 2006; Kosaka et al. 2009; Hu et al. 2018; P. Xu et al. 2019):

$$CP = -\left(\frac{f}{\sigma} v'T' \frac{\partial \bar{u}}{\partial p} - \frac{f}{\sigma} u'T' \frac{\partial \bar{v}}{\partial p} \right) \quad (1)$$

Here, u, v and T denote the zonal wind, meridional wind and temperature, respectively. Overbars indicate the climatological JJA mean and primes denote the perturbations regressed onto the normalized HETI. f is the Coriolis parameter, p pressure, and σ the stability parameter $\sigma = \frac{R\bar{T}}{C_p p} - \frac{d\bar{T}}{dp}$, with R the gas constant and C_p the specific heat at constant pressure. Positive *CP* means the conversion of available potential energy from the mean flow to the teleconnection pattern.

To measure the net contribution of *CP* to the maintenance of the monthly anomalies associated with the HET, we evaluate the time scales:

$$\tau_{CP} = \frac{\langle [APE] \rangle}{\langle [CP] \rangle} \quad (2)$$

where the $\langle\ \rangle$ represents either the area average over the Northern Hemisphere 5º–85°N or the wave train domain 45º–75°N, 30°W–150°E and [ ] indicates vertical integration. $APE = \frac{RT'^2}{2\sigma p}$ is available potential energy associated with the HET. τ_{CP} denotes how long it takes the observed available potential energy anomalies to be fully replenished through *CP*.

Figure 4 shows the *CP* and its two terms, i.e., $-\frac{f}{\sigma} v'T' \frac{\partial \bar{u}}{\partial p}$ (term 1) and $\frac{f}{\sigma} u'T' \frac{\partial \bar{v}}{\partial p}$

Accepted for publication in *Journal of Climate*. DOI 10.1175/JCLI-D-19-0362.1.

(term 2), integrated from the surface to 100 hPa, associated with the HET. *CP* is characterized by alternatively positive and negative values over the high-latitude Eurasian continent (Fig. 4a). However, positive *CP* is obviously larger than negative *CP*, indicating that the wave train can extract available potential energy from the mean flow to maintain or reinforce itself through baroclinic energy conversion. The available potential energy of the perturbations can be replenished within one week over the Northern Hemisphere (4.04 days), and the baroclinic energy conversion is more efficient when focused on the wave train domain (only 3.11 days). Since the conversion time-scale is much shorter than one month, the HET can be easily maintained against dissipative processes.

The predominant term in *CP* is $-\frac{f}{\sigma}v'T'\frac{\partial \bar{u}}{\partial p}$ (Fig. 4b vs. Fig. 4c), and its distribution resembles well that for *CP* (Fig. 4a). The area-averaged value of this term is 0.0045 W m^{-2} over the Northern Hemisphere and 0.0207 W m^{-2} over the wave train domain, larger than those of the total *CP* (0.0043 W m^{-2} over the Northern Hemisphere and 0.0186 W m^{-2} over the wave train domain). The other term, $\frac{f}{\sigma}u'T'\frac{\partial \bar{v}}{\partial p}$, on the other hand, is very weak (Fig. 4c). Therefore, we focus on the first term ($-\frac{f}{\sigma}v'T'\frac{\partial \bar{u}}{\partial p}$) of *CP* in the following.

Figure 5 shows the vertical section of *CP* and $-\frac{f}{\sigma}v'T'\frac{\partial \bar{u}}{\partial p}$ along 63°N, which is approximately the latitude of strongest positive and negative vertically-integrated values (Figs. 4a and 4b). For each pressure level, *CP* is almost same as $-\frac{f}{\sigma}v'T'\frac{\partial \bar{u}}{\partial p}$, consistent with the integrated results (Fig. 4). Most of the baroclinic energy conversion occurs below 250 hPa, with the maximum amplitudes appearing at mid-troposphere (400 hPa). Positive *CP*

Accepted for publication in *Journal of Climate*. DOI 10.1175/JCLI-D-19-0362.1.

256 also extends downward to the lower troposphere and shows an amplitude maximum at 925
257 hPa. Negative *CP*, on the other hand, only appears over the mid-troposphere. In addition,
258 there are also some cells above 250 hPa but the values are very weak.

259 Figure 6 shows $-\frac{f}{\sigma}v'T'\frac{\partial\bar{u}}{\partial p}$ integrated from 700−300 hPa and 1000−700 hPa, to
260 investigate baroclinic energy conversion in the mid-troposphere and lower troposphere. The
261 distributions of $-\frac{f}{\sigma}v'T'\frac{\partial\bar{u}}{\partial p}$ at the mid and lower troposphere both resemble the wave-like
262 distribution for the whole troposphere (Fig. 4b), though both the positive and negative values
263 in the mid-troposphere appear to be larger than those in the lower-troposphere. $-\frac{f}{\sigma}v'T'\frac{\partial\bar{u}}{\partial p}$
264 averaged over the Northern Hemisphere and the wave train domain for the mid and lower
265 troposphere are listed in Tab. 1. $-\frac{f}{\sigma}v'T'\frac{\partial\bar{u}}{\partial p}$ averaged over the wave train domain is 0.0106
266 W m^{-2} for the mid troposphere and 0.0100 W m^{-2} for the lower troposphere. Therefore, we
267 can conclude that this term or baroclinic energy conversion in the mid-troposphere and lower
268 troposphere equivalently maintains or reinforces the HET.

269 $-\frac{f}{\sigma}v'T'\frac{\partial\bar{u}}{\partial p}$ is determined by both the disturbance structure and the basic state, i.e.,
270 $v'T'$ and $-\frac{f}{\sigma}\frac{\partial\bar{u}}{\partial p}$. Figure 7 shows the vertical cross section of these two components along
271 63°N. The wave-like distribution of $v'T'$ resembles that of *CP* (Figs. 7a and 5), but with
272 opposite-signed cells below and above 250 hPa. For those below 250 hPa, positive values are
273 obviously greater than the negative ones, contributing to the positive *CP*. Positive values also
274 extend downward to the surface, while negative values in the low levels are very weak. On

Accepted for publication in *Journal of Climate*. DOI 10.1175/JCLI-D-19-0362.1.

the other hand, the basic state component shows two large bands in the lower troposphere and mid-troposphere, respectively (Fig. 7b), consistent with the most efficient energy conversion there. In addition, $-\frac{f}{\sigma}\frac{\partial \bar{u}}{\partial p}$ is very weak above 250 hPa, leaving weak values of *CP* there, although $v'T'$ is strong (Figs. 7 and 5).

Figure 8 further looks into the vertical cross section of the disturbance term. The vertical cross section of meridional wind anomalies (v') clearly exhibits an equivalent-barotropic teleconnection pattern, with maxima of anomalies at 250 hPa. These anomalies extend downwards to the surface, except over the Northeast Asia, where the anomalies are weak at the low level possibly due to the topography. Similar to 250 hPa, the strongest positive and negative meridional wind anomalies for each level appear at about 45°E and 90°E, respectively. However, these positive anomalies tilt westward with height, while the negative ones tilt slightly eastward in the troposphere. The temperature anomalies (T') also exhibit equivalent-barotropic features, showing anomalous centers in the upper and lower troposphere, respectively. T' exhibits opposite-signed anomalies below and above 250 hPa, resulting in opposite-signed $v'T'$ below and above this level (Fig. 7a). In the troposphere, the positive T' between 45°E and 90°E is strongest and extends clearly to the surface. This temperature anomaly is well associated with the anticyclonic anomaly indicated by the positive and negative meridional wind anomalies. However, a closer inspection indicates that v' leads T' not exactly by 1/4 phase in the troposphere, especially in the lower levels, leading to non-zero values for $v'T'$, an issue discussed further in the next section.

Figure 9 shows the vertical cross section of the components associated with the basic

Accepted for publication in *Journal of Climate*. DOI 10.1175/JCLI-D-19-0362.1.

state ($-\frac{f}{\sigma}\frac{\partial \bar{u}}{\partial p}$) along 63°N. The term $\frac{f}{\sigma}$ shows its largest values in the lower troposphere (Fig. 9a), which results from smallest values of σ, suggesting that the atmospheric stratification is more unstable in the lower troposphere. The distribution of $\frac{f}{\sigma}$ corresponds well to the distribution of land and sea in the lower troposphere. There are larger values over the Eurasian continent 0°−150°E and North America 165°W−95°W, but smaller values over the North Pacific 150°E−165°W and North Atlantic 95°W−0°. This is because land warms up faster than the ocean during summer and the temperature in the lower troposphere is easily affected by the surface sensible heat flux. Therefore, the atmospheric stratification over land is more unstable than that over the ocean. $\frac{f}{\sigma}$ is also relatively large and uniform in the mid-troposphere around 400 hPa, consistent with large *CP* there. The two large bands of $\frac{f}{\sigma}$ correspond well to those of the basic state (Fig. 7b), indicating that $\frac{f}{\sigma}$ plays an important role in the basic state component. In addition, $\frac{f}{\sigma}$ becomes very weak above 250 hPa, due to the strong stability of atmosphere in the stratosphere. As a result, $-\frac{f}{\sigma}v'T'\frac{\partial \bar{u}}{\partial p}$ and *CP* are very weak there (Fig. 5).

σ is determined by two components: $\frac{R\bar{T}}{C_p p}$ and $\frac{\partial \bar{T}}{\partial p}$. As the air density decreases with height, the term $\frac{R\bar{T}}{C_p p}$ expectedly increases, and exhibits nearly uniform values at each level (Fig. 9b). Even for the lower troposphere, where the temperature and pressure may depend appreciably on the distribution of land and sea, this term is almost constant in the zonal

Accepted for publication in *Journal of Climate*. DOI 10.1175/JCLI-D-19-0362.1.

direction. For instance, $\frac{R\overline{T}}{C_p p}$ are very similar over the Eurasian continent and North Pacific at 925 hPa, being 8.80×10^{-4} K Pa^{-1} and 8.70×10^{-4} K Pa^{-1} averaged over 63°N, 0°−150°E and 63°N, 150°E−165°W, respectively. Therefore, this term can contribute to smallest values of σ in the lower troposphere, but cannot explain the distinct land-sea distribution of σ.

The term $\frac{\partial\overline{T}}{\partial p}$ basically increases with height in the troposphere and shows its largest values in the mid-upper levels (Fig. 9c). These large values, together with $\frac{R\overline{T}}{C_p p}$, which increases with height (Fig. 9b), lead to relatively weaker σ and resultant greater $\frac{f}{\sigma}$ around 400 hPa (Fig. 9a). In the lower troposphere, on the other hand, the term $\frac{\partial\overline{T}}{\partial p}$ shows a distinct land-sea distribution, being larger over the continents than the oceans. For example, the difference in climatological mean temperature between 1000 hPa and 850 hPa averaged over the Eurasian continent 63°N, 0°−150°E is 8.95 K, 76% larger than that over the North Atlantic 63°N, 95°W−0° (5.09 K). This term is associated with the basic state of temperature, which decreases with height, as expected (Fig. 9d). The basic state of temperature in the lower troposphere also exhibits a distinct land-sea contrast, with higher temperature over the continents than the oceans. These features favor lower stability of the atmospheric stratification over the continents.

On the other hand, the climatological zonal winds increase uniformly with height below 250 hPa and decrease above this level (Fig. 9f), thus the term $-\frac{\partial\overline{u}}{\partial p}$ is almost a constant below 250 hPa (Fig. 9e), with a value of around 1.0×10^{-4} m Pa^{-1} s^{-1}. This result indicates

Accepted for publication in *Journal of Climate*. DOI10.1175/JCLI-D-19-0362.1.

that the basic flow in the high latitudes shows not only weak zonal and meridional shear (Fig. 1a), but also weak vertical shear (Fig. 9e). This is distinctly different from the basic flow in the mid-latitudes, where $-\frac{\partial \bar{u}}{\partial p}$ shows very strong values below and above the westerly jet. Therefore, compared to $-\frac{\partial \bar{u}}{\partial p}$, the atmospheric stability σ plays a more important role in the basic state component of *CP* (Figs. 9a and 9e vs. Fig. 7b).

The results in this section indicate that the HET can be maintained by extracting available potential energy from the basic flow, i.e., the baroclinic energy conversion, *CP*. *CP* is efficient not only in the mid-troposphere, but also in the lower troposphere. The perturbations associated with the HET and the basic state both significantly contribute to positive *CP*. Especially, the atmospheric stability associated with the basic state of temperature in the lower troposphere is important. This is distinctly different from the mid-latitude teleconnection, which greatly relies on the basic state of the zonal wind in mid-upper levels. The results in this section are obtained by the vertical cross section of these components. The horizontal distribution of these components in the mid-troposphere and lower troposphere is investigated further in the subsequent section.

4 Baroclinic energy conversion *CP* associated with the HET in the mid-troposphere and lower troposphere

The results in the preceding section indicate that the *CP* associated with the HET features two maxima in amplitude at 400 hPa and 925 hPa, respectively. In this section, we further explore the horizontal distribution of baroclinic energy conversion at these two levels.

Accepted for publication in *Journal of Climate*. DOI 10.1175/JCLI-D-19-0362.1.

353 Figure 10 shows the distributions of $-\frac{f}{\sigma}v'T'\frac{\partial \bar{u}}{\partial p}$ and each component associated with

354 this term at 400 hPa. $-\frac{f}{\sigma}v'T'\frac{\partial \bar{u}}{\partial p}$ exhibits alternating positive and negative values (Fig.

355 10a). The positive values are obviously larger than the negative ones. The maximum positive

356 value (at 63°N, 52.5°E) is 1.07×10^{-4} W m^{-2}, 70% higher than the maximum negative value

357 (at 64.5°N, 78°E; -6.13×10^{-5} W m^{-2}). The higher positive values are dominated by the

358 larger positive values of the disturbance term $v'T'$ (Fig. 10c), the distribution of which

359 resembles $-\frac{f}{\sigma}v'T'\frac{\partial \bar{u}}{\partial p}$. $v'T'$ at 63°N, 52.5°E is 2.00 m K s^{-1}, 50% higher than that at

360 64.5°N, 78°E (−1.33 m K s^{-1}). The pattern of $v'T'$ is associated with the configuration of

361 v' and T'. v' leads T' roughly by 1/4 phase (Fig. 10e and Fig. 12a), which can be

362 explained by the association between the anticyclonic/cyclonic anomaly and warmer/cooler

363 temperatures. However, a careful scrutiny shows that the center of positive v' appears over

364 positive T', rather than at the zero contour (Fig. 12a). The configuration of v' and T' is

365 important for the sign of $v'T'$: The total sum of $v'T'$ is positive (negative) if v' leads or

366 lags T' by less (more) than 1/4 phase, and it is zero if v' leads or lags T' exactly by 1/4

367 phase. Therefore, though $v'T'$ shows alternative positive and negative values, the positive

368 ones are stronger than the negative ones (Fig. 10c).

369 On the other hand, the term associated with the basic state ($-\frac{f}{\sigma}\frac{\partial \bar{u}}{\partial p}$) is strongest over

370 mid-latitude Eurasia and the North Atlantic, and shows another relatively high amplitude belt

371 over high-latitude Eurasia (Fig. 10b). For the mid-latitude Eurasia and North Atlantic, the

372 basic state of zonal wind ($-\frac{\partial \bar{u}}{\partial p}$) plays a dominant role due to the existence of the westerly jet

Accepted for publication in *Journal of Climate*. DOI 10.1175/JCLI-D-19-0362.1.

(Figs. 10b and 10d). However, over high-latitude Eurasia, $-\frac{\partial \bar{u}}{\partial p}$ is much smaller. By contrast, the stability parameter σ is smaller over high-latitude Eurasia (Fig. 10f) than in the mid-latitudes. Besides, the Coriolis parameter f over the high latitudes is larger than that in the mid-latitudes, which is 12.99×10^{-5} s^{-1} for 63°N and 9.37×10^{-5} s^{-1} for 40°N. As a result, $\frac{f}{\sigma}$ in the high latitudes is larger than that in the mid-latitudes. Therefore, $\frac{f}{\sigma}$ is important for the energy conversion in the high latitudes, while for the mid-latitudes, the energy conversion is more favored by the basic state of zonal wind.

Figure 11 shows the distributions of $-\frac{f}{\sigma}v'T'\frac{\partial \bar{u}}{\partial p}$ and each component associated with this term at 925 hPa. Positive $-\frac{f}{\sigma}v'T'\frac{\partial \bar{u}}{\partial p}$ mainly appears over 50°−72.5°N, 40°−70°E, indicating that baroclinic energy conversion is most efficient there (Fig. 11a). $-\frac{f}{\sigma}v'T'\frac{\partial \bar{u}}{\partial p}$ over the other regions is very weak. The distribution of $v'T'$ resembles $-\frac{f}{\sigma}v'T'\frac{\partial \bar{u}}{\partial p}$ (Fig. 11c), confirming its important role in in determining the pattern of *CP*. Positive $v'T'$ results from the strong positive v' and positive T' there (Fig. 11e). Compared to 400 hPa, v' and T' are more in phase at 925 hPa (Figs. 11e and 12b), i.e., the anomalous southerly flow basically corresponds to positive temperature anomalies and the anomalous northerly flow corresponds to the negative temperature anomalies. This is because the meridional gradient of mean temperature in the lower troposphere is larger than that in the mid-troposphere: the value averaged over the wave train domain is -2.02×10^{-6} K m^{-1} at 925 hPa, stronger than that at 400 hPa (-1.31×10^{-6} K m^{-1}), and thus the temperature anomalies in the lower

Accepted for publication in *Journal of Climate*. DOI 10.1175/JCLI-D-19-0362.1.

troposphere are greatly affected by the anomalous meridional advection of mean temperature.

The basic state term ($-\frac{f}{\sigma}\frac{\partial \bar{u}}{\partial p}$) at this level shows a distinct land-sea distribution, with greater values over the continents than the oceans (Fig. 11b). This is mainly induced by the distinct land-sea contrast of σ (Figs. 11b and 11f). For the Eurasian continent, the distribution of $-\frac{f}{\sigma}\frac{\partial \bar{u}}{\partial p}$ resembles σ (Fig. 11f), suggesting that σ significantly contributes to $-\frac{f}{\sigma}\frac{\partial \bar{u}}{\partial p}$. $-\frac{\partial \bar{u}}{\partial p}$ is stronger over the high-latitudes than the mid-latitudes in the Eurasian continent (Fig. 11d), possibly due to the thermal contrast between the Eurasian continent and Arctic Sea through thermal wind relationship. In addition, compared to that at 400 hPa (Fig. 10f), σ at 925 hPa is much weaker, suggesting that it plays a more important role in $-\frac{f}{\sigma}\frac{\partial \bar{u}}{\partial p}$ (Fig. 11f). This is because the atmosphere in the low levels is more easily affected by surface sensible heating, resulting in lower atmospheric stability. Therefore, we can confirm that the lower-tropospheric atmospheric stability plays an important role in energy conversion, which has been shown in the preceding section.

It is notable that the reanalysis data are artificial under the surface. Fortunately, positive $-\frac{f}{\sigma}v'T'\frac{\partial \bar{u}}{\partial p}$ at 925 hPa appears over the plains (Fig. 11a) and the reanalysis data there should be reliable. We also used the NCEP/ NCAR reanalysis data and the JRA-55 data to repeat these analyses and obtained similar results.

In summary, the results in this section confirm that the configuration of v' and T' plays an important role in energy conversion associated with the high-latitude teleconnection

Accepted for publication in *Journal of Climate*. DOI 10.1175/JCLI-D-19-0362.1.

411 pattern. Particularly, in the lower troposphere, v' and T' are more in phase due to the
412 larger meridional gradient of mean temperature. In addition, the basic state plays a key role in
413 the baroclinic energy conversion for both the mid-troposphere and lower troposphere. On one
414 hand, the stability parameter is small and the Coriolis parameter is large in the high latitudes,
415 favoring strong baroclinic energy conversion. Especially, in the lower troposphere, the
416 stability parameter exhibits a clear land-sea contrast, with smaller values over the continents
417 than the oceans. On the other hand, although the vertical shear of the mean zonal wind is
418 weak in both the mid- and lower troposphere over high-latitude Eurasia, in the low levels it is
419 relatively larger in the high latitudes than the mid-latitudes. All these features determine that
420 the lower-tropospheric energy conversion occurs in the high latitudes of the Eurasian
421 continent.

422 ## 5 Conclusions and discussion

423 In this study, we confirmed the existence of a teleconnection pattern over the
424 high-latitude Eurasian continent in summer, and confirmed, using the same analysis
425 procedure as Kosaka et al. (2009), that this teleconnection pattern can be maintained through
426 baroclinic energy conversion, as has been suggested in previous studies (Xie and Kosaka
427 2016; P. Xu et al. 2019). We called this teleconnection pattern HET (High-latitude Eurasian
428 Teleconnection), to emphasize the unique role of the basic state over the high latitudes of the
429 Eurasian continent in maintaining the teleconnection, which is also the main focus of this
430 study.

431 It is found that the baroclinic energy conversion is most efficient in the mid and lower
432 troposphere. The baroclinic energy conversion in these two layers contributes equivalently to

Accepted for publication in *Journal of Climate*. DOI10.1175/JCLI-D-19-0362.1.

433 the maintenance of HET. Further analysis indicates that baroclinic energy conversion is
434 dominated by the stability parameter and vertical gradient of zonal winds. The stability
435 parameter is small in both the mid and lower troposphere over the high latitudes of the
436 Eurasian continent, favoring baroclinic energy conversion. On the other hand, the vertical
437 gradient of zonal winds is uniform in the entire troposphere over the high latitudes of the
438 Eurasian continent. However, the vertical gradient of zonal winds is relatively larger around
439 the northern edge of the Eurasian continent in the lower troposphere, resulting in the strong
440 baroclinic energy conversion, together with the stability parameter. Furthermore, the
441 disturbances associated with the HET also favor baroclinic energy conversion, by showing
442 positive values of $v'T'$ larger than the negative ones. In the lower troposphere, particularly,
443 positive values of $v'T'$ are much larger than the negative ones, and this is very important for
444 baroclinic energy conversion. Finally, the Coriolis parameter, which is larger in the high
445 latitudes, also contributes to the strong baroclinic energy conversion in the high latitudes of
446 the Eurasian continent, as expected.

447 The present results indicate that the basic state plays a key role in maintaining the HET.
448 The role of the basic state can be summarized as follows. First, the low stability in the mid
449 troposphere over high-latitude Eurasia makes the baroclinic energy conversion there
450 comparable to, albeit weaker than, the conversion in the mid-latitudes, despite the very strong
451 gradient of zonal winds in the latter region (Fig. 10). Second, in the lower troposphere, the
452 stability is also low over the Eurasian continent due to surface sensible heating, and the
453 vertical gradient of zonal winds is relatively larger over high-latitude Eurasia possibly due to
454 the thermal contrast between the Eurasian continent and Arctic Sea during summer, both

Accepted for publication in *Journal of Climate*. DOI 10.1175/JCLI-D-19-0362.1.

favoring strong baroclinic energy conversion (Fig. 11). Finally, the strong contrast between warm lands and cool seas around the northern edge of the Eurasian continent during summer provides a good condition for inducing the structure of disturbances that favors strong positive baroclinic energy conversion, i.e., southerly (northerly) anomalies resulting in warmer (cooler) air temperatures (Fig. 11).

Considering the important role of the basic state, we speculate that the high latitudes of the Eurasian continent could be a unique region for pure high-latitude teleconnections. On the one hand, although the basic state can also favor baroclinic energy conversion over the high latitudes of North America (Fig. 11b), the longitudinal scope is much smaller and thus it prevents the appearance of teleconnections there. On the other hand, in the Southern Hemisphere during the boreal summer, we found that teleconnection patterns exist over the high latitudes (not shown), possibly favored by baroclinic energy conversion roughly around 60°S. However, these high-latitude teleconnections are closely related to those along the upper-tropospheric westerly jet in the Southern Hemisphere, unlike the independence of mid- and high-latitude teleconnections shown in the present results. We attribute this difference between the Northern and Southern Hemisphere to the relatively poleward location of the Southern Hemisphere jet. For instance, for the austral summer, Lin (2019) identified a stationary teleconnection in the South Atlantic and South Indian Ocean (roughly around 50°S), and attributed it to the strong Southern Hemisphere westerly jet there. Therefore, the mechanism for the teleconnection patterns in the Southern Hemisphere might be more complicated and require further investigation. In addition, this study indicates that the HET is relatively independent of the mid-latitude SRP. Therefore, it could be expected that different

Accepted for publication in *Journal of Climate*. DOI 10.1175/JCLI-D-19-0362.1.

configurations of the HET and SRP would result in different climate effects over Eurasia, which is another interesting topic for future study.

Acknowledgments

We thank Dr. Hisashi Nakamura and two anonymous reviewers for their valuable comments. This work was supported by the National Natural Science Foundation of China (Grant No. 41721004), the Natural Science Foundation of Jiangsu Province (No. BK20190500), and the Fundamental Research Funds for the Central Universities (No. 2013B18020068).

Accepted for publication in *Journal of Climate*. DOI 10.1175/JCLI-D-19-0362.1.

References

Ambrizzi, T., B. J. Hoskins, and H.-H. Hsu, 1995: Rossby wave propagation and teleconnection patterns in the austral winter. *J. Atmos. Sci.*, **52**, 3661–3672, https://doi.org/10.1175/1520-0469(1995)052<3661:RWPATP>2.0.CO;2.

Bladé, I., B. Liebmann, D. Fortuny, and G. J. van Oldenborgh, 2012: Observed and simulated impacts of the summer NAO in Europe: Implications for projected drying in the Mediterranean region. *Climate Dyn.*, **39**, 709–727, https://doi.org/10.1007/s00382-011-1195-x.

Branstator, G. and H. Teng, 2017: Tropospheric waveguide teleconnections and their seasonality. *J. Atmos. Sci.*, **74**, 1513–1532, https://doi.org/10.1175/JAS-D-16-0305.1.

Cassou, C., L. Terray, and A.S. Phillips, 2005: Tropical Atlantic influence on European heat waves. *J. Climate*, **18**, 2805–2811.

Chen, G., and R. Huang, 2012: Excitation mechanisms of the teleconnection patterns affecting the July precipitation in northwest China. *J. Climate*, **25**, 7834–7851, https://doi.org/10.1175/JCLI-D-11-00684.1.

Dee, D. P., and Coauthors, 2011: The ERA-Interim reanalysis: Configuration and performance of the data assimilation system. *Quart. J. Roy. Meteor. Soc.*, **137**, 553–597, https://doi.org/10.1002/qj.828.

Ding, Q., and B. Wang, 2005: Circumglobal teleconnection in the northern hemisphere summer. *J. Climate*, **18**, 3483–3505.

Ding, Q., B. Wang, J. M. Wallace, and G. Branstator, 2011: Tropical–extratropical

Accepted for publication in *Journal of Climate*. DOI 10.1175/JCLI-D-19-0362.1.

teleconnections in boreal summer: Observed interannual variability. *J. Climate*, **24**, 1878–1896, https://doi.org/10.1175/2011JCLI3621.1.

Enomoto, T., B. J. Hoskins, and Y. Matsuda, 2003: The formation mechanism of the Bonin high in August. *Quart. J. Roy. Meteor. Soc.*, **129**, 157–178, https://doi.org/10.1256/qj.01.211.

Feldstein, S. B., 2007: The dynamics of the North Atlantic Oscillation during the summer season. *Quart. J. Roy. Meteor. Soc.*, **133**, 1509–1518.

Folland, C. K., J. Knight, H. W. Linderholm, D. Fereday, S. Inesen, and J. W. Hurrell, 2009: The summer North Atlantic Oscillation: Past, present, and future. *J. Climate*, **22**, 1082–1103, https://doi.org/10.1175/2008JCLI2459.1.

Fukutomi, Y., K. Masuda, and T. Yasunari, 2004: Role of storm activity in the interannual seesaw of summer precipitation over northern Eurasia. *J. Geophys. Res.*, **109**, D02109.

Greatbatch, R. J. and P. Rong, 2006: Discrepancies between different Northern Hemisphere summer atmospheric data products. *J. Climate*, **19**, 1261–1273, https://doi.org/10.1175/JCLI3643.1.

Greatbatch, R. J., X. Sun, and X. Yang, 2013: Impact of variability in the Indian summer monsoon on the East Asian summer monsoon. *Atmos. Sci. Lett.*, **14**, 14–19.

Hong, X., and R. Lu, 2016: The meridional displacement of the summer Asian jet, Silk Road pattern, and tropical SST anomalies. *J. Climate*, **29**, 3753–3766, https://doi.org/10.1175/JCLI-D-15-0541.1.

Hong, X., R. Lu, and S. Li, 2017: Amplified summer warming in Europe–West Asia and Northeast Asia after the mid-1990s. *Environ. Res.*

Accepted for publication in *Journal of Climate*. DOI 10.1175/JCLI-D-19-0362.1.

Lett., **12**, 094007, https://doi.org/10.1088/1748-9326/aa7909.

Hong, X., R. Lu, and S. Li, 2018: Differences in the Silk Road pattern and its relationship to the North Atlantic Oscillation between early and late summers. *J. Climate*, **31**, 9283–9292, doi:10.1175/JCLI-D-18-0283.1.

Hoskins, B. J., and D. J. Karoly, 1981: The steady linear response of a spherical atmosphere to thermal and orographic forcing. *J. Atmos. Sci.*, **38**, 1179–1196, https://doi.org/10.1175/1520-0469(1981)038<1179:TSLROA>2.0.CO;2.

Hoskins, B. J., and T. Ambrizzi, 1993: Rossby wave propagation on a realistic longitudinally varying flow. *J. Atmos. Sci.*, **50**, 1661–1671, https://doi.org/10.1175/1520-0469(1993)050<1661:RWPOAR>2.0.CO;2.

Hu, K., G. Huang, R. Wu, and L. Wang, 2018: Structure and dynamics of a wave train along the wintertime Asian jet and its impact on East Asian climate. *Climate Dyn.*, **51**, 4123–4137, https://doi.org/10.1007/s00382-017-3674-1.

Huang, R., and F. Sun, 1992: Impacts of the tropical western Pacific on the East Asia summer monsoon. *J. Meteor. Soc. Japan*, **70**, 243–256.

Iwao, K., and M. Takahashi, 2006: Interannual change in summertime precipitation over northeast Asia. *Geophys. Res. Lett.*, **33**, L16703.

Iwao, K., and M. Takahashi, 2008: A precipitation seesaw mode between Northeast Asia and Siberia in summer caused by Rossby waves over the Eurasian continent. *J. Climate*, **21**, 2401–2419, https://doi.org/10.1175/2007JCLI1949.1.

Kalnay, E., and Coauthors, 1996: The NCEP/NCAR 40-year reanalysis project. *Bull. Amer.*

Accepted for publication in *Journal of Climate*. DOI 10.1175/JCLI-D-19-0362.1.

552 *Meteor. Soc.*, 77, 437–470.
553 Kobayashi, S., and Coauthors, 2015: The JRA-55 reanalysis: General specifications and basic
554 characteristics. *J. Meteor. Soc. Japan*, **93**, 5–48.
555 Kosaka, Y., S.-P. Xie, and H. Nakamura, 2011: Dynamics of interannual variability in
556 summer precipitation over East Asia. *J. Climate*, **24**, 5435–5453.
557 Kosaka, Y., and H. Nakamura, 2006: Structure and dynamics of the summertime
558 Pacific–Japan teleconnection pattern. *Quart. J. Roy. Meteor. Soc.*, **132**, 2009–2030.
559 Kosaka, Y., H. Nakamura, M. Watanabe, and M. Kimoto, 2009: Analysis on the dynamics of
560 a wave-like teleconnection pattern along the summertime Asian jet based on a reanalysis
561 dataset and climate model simulations. *J. Meteor. Soc. Japan*, **87**, 561–580,
562 https://doi.org/10.2151/jmsj.87.561.
563 Lee, E., J. Jhun, and C. Park, 2005: Remote connection of the Northeast Asian summer
564 rainfall variation revealed by a newly defined monsoon index. *J. Climate*, **18**,
565 4381–4393, https://doi.org/10.1175/JCLI3545.1.
566 Li, J., and C. Ruan, 2018: The North Atlantic–Eurasian teleconnection in summer and its
567 effects on Eurasian climates. *Environ. Res. Lett.*, **13**, 024007,
568 https://doi.org/10.1088/1748-9326/aa9d33.
569 Li, X., and R. Lu, 2017: Extratropical factors affecting the variability in summer Precipitation
570 over the Yangtze River basin, China. *J. Climate*, **30**, 8357–8374,
571 https://doi.org/10.1175/JCLI-D-16-0282.1.
572 Li, X., and R. Lu, 2018: Subseasonal change in the seesaw pattern of precipitation between
573 the Yangtze River basin and the tropical western North Pacific during summer. *Adv.*

Accepted for publication in *Journal of Climate*. DOI 10.1175/JCLI-D-19-0362.1.

574 *Atmos. Sci.*, **35(10)**, 1231–1242, https://doi.org/10.1007/s00376-018-7304-6.
575 Lin, Z., 2014: Intercomparison of the impacts of four summer teleconnections over Eurasia
576 on East Asian rainfall. *Adv. Atmos. Sci.*, **31(6)**, 1366–1376,
577 https://doi.org/10.1007/s00376-014-3171-y.
578 Lin, Z., 2019: The South Atlantic–South Indian Ocean pattern: a zonally oriented
579 teleconnection along the southern Hemisphere westerly jet in austral summer.
580 *Atmosphere*, **10(5)**, 259, https://doi.org/10.3390/atmos10050259.
581 Lin, Z., R. Lu, and R. Wu, 2017a: Weakened impact of the Indian early summer monsoon on
582 North China rainfall around the late 1970s: role of basic-state change. *J. Climate*, **30**,
583 7991–8005, https://doi.org/10.1175/JCLI-D-17-0036.1.
584 Lin, Z., F. Liu, B. Wang, R. Lu, and X. Qu, 2017b: Southern European rainfall reshapes the
585 early-summer circumglobal teleconnection after the late 1970s. *Climate Dyn.*, **48**,
586 3855–3868, https://doi.org/10.1007/s00382-016-3306-1.
587 Lu, R., 2004: Associations among the components of the East Asian summer monsoon system
588 in the meridional direction. *J. Meteor. Soc. Japan*, **82**, 155–165.
589 Lu, R., and B. Dong, 2001: Westward extension of North Pacific subtropical high in summer.
590 *J. Meteor. Soc. Japan*, **79**, 1229–1241.
591 Lu, R., J. H. Oh, and B. J. Kim, 2002: A teleconnection pattern in upper-level meridional
592 wind over the North African and Eurasian continent in summer. *Tellus*, **54A**, 44–55.
593 Nakamura, H., and T. Fukamachi, 2004: Evolution and dynamics of summertime blocking
594 over the Far East and the associated surface Okhotsk high. *Quart. J. Roy. Meteor. Soc.*,
595 **130**, 1213–1233.

Accepted for publication in *Journal of Climate*. DOI 10.1175/JCLI-D-19-0362.1.

596 Nitta, T., 1986: Long-term variations of cloud amount in the western Pacific region. *J. Meteor.*
597 *Soc. Japan*, **64**, 373–390.
598 Nitta, T., 1987: Convective activities in the tropical western Pacific and their impact on the
599 Northern Hemisphere summer circulation. *J. Meteor. Soc. Japan*, **65**, 373–390,
600 https://doi.org/10.2151/jmsj1965.65.3_373.
601 North, G. R., L. B. Thomas, F. C. Robert, and J. M. Fanthune, 1982: Sampling errors in the
602 estimation of empirical orthogonal functions. *Mon. Wea. Rev.*, **110**, 699–706,
603 https://doi.org/10.1175/1520-0493(1982)110<0699:SEITEO>2.0.CO;2.
604 Sato, N., and M. Takahashi, 2006: Dynamical processes related to the appearance of
605 quasi-stationary waves on the subtropical jet in the midsummer Northern Hemisphere. *J.*
606 *Climate*, **19**, 1531–1544, https://doi.org/10.1175/JCLI3697.1.
607 Song, F., T. Zhou, and L. Wang, 2013: Two modes of the Silk Road pattern and their
608 interannual variability simulated by LASG/IAP AGCM SAMIL2.0. *Adv. Atmos.*
609 *Sci.*, **30**, 908–921, https://doi.org/10.1007/s00376-012-2145-1.
610 Sun, J., and H. Wang, 2012: Changes of the connection between the summer North Atlantic
611 Oscillation and the East Asian summer rainfall. *J. Geophys. Res.*, **117**, D08110,
612 https://doi.org/10.1029/2012JD017482.
613 Takaya, K., and H. Nakamura, 2001: A formulation of a phase-independent wave-activity
614 flux for stationary and migratory quasigeostrophic eddies on a zonally varying basic flow.
615 *J. Atmos. Sci.*, **58,** 608–627.
616 Wakabayashi, S., and R. Kawamura, 2004: Extraction of major teleconnection patterns
617 possibly associated with the anomalous summer climate in Japan. *J. Meteor. Soc.*

Accepted for publication in *Journal of Climate*. DOI 10.1175/JCLI-D-19-0362.1.

618 *Japan*, **82**, 1577–1588, https://doi.org/10.2151/jmsj.82.1577.

619 Wang, Z., S. Yang, N. Lau, and A. Duan, 2018: Teleconnection between summer NAO and
620 east China rainfall variations: A bridge effect of the Tibetan Plateau. *J. Climate*, **31**,
621 6433–6444, https://doi.org/10.1175/JCLI-D-17-0413.1.

622 Wang, Y., 1992: Effects of blocking anticyclones in Eurasia in the rainy season (meiyu/baiu
623 season). *J. Meteor. Soc. Japan*, **70**, 929–951.

624 Wu, R., 2002: A mid- latitude Asian circulation anomaly pattern in boreal summer and its
625 connection with the Indian and East Asian summer monsoons. *Int. J. Climatol*., **22**,
626 1879–1895.

627 Wulff, C. O., R. J. Greatbatch, D. I. V. Domeisen, G. Gollan, and F. Hansen, 2017: Tropical
628 forcing of the summer East Atlantic pattern. *Geophys. Res. Lett.*, **44**, 11166–11173.

629 Xie, S., and Y. Kosaka, 2016: Interannual variability and predictability of summer climate
630 over the Northwest Pacific and East Asia. *Dynamics and Predictability of Large-Scale,*
631 *High-Impact Weather and Climate Events*, J. Li, R. Swinbank, R. Grotjahn, and H.
632 Volkert, Ed., Cambridge University Press, 333–342.

633 Xu, K., R. Lu, B. Kim, J. Park, J. Mao, J. Byon, R. Chen, and E. Kim, 2019: Large-scale
634 circulation anomalies associated with extreme heat in South Korea and southern–central
635 Japan. *J. Climate*, **32**, 2747–2759, https://doi.org/10.1175/JCLI-D-18-0485.1.

636 Xu, P., L. Wang, and W. Chen, 2019: The British–Baikal corridor: A teleconnection pattern
637 along the summertime polar front jet over Eurasia. *J. Climate*, **32**,
638 877–896, https://doi.org/10.1175/JCLI-D-18-0343.1.

639 Yang, X., 1992: Observational study of teleconnecuons in the geopotentml height during the

Accepted for publication in *Journal of Climate*. DOI 10.1175/JCLI-D-19-0362.1.

Northern Hermsphere summer. *Chinese J. Atmos. Sci.*, **16(5)**, 513–521. (in Chinese)

Yang, X., and S. Huang, 1992: Horizontal structure and energetics of Northern Hemisphere summertime teleconnection patterns. *J. Meteor. Sci.*, **12(2)**, 119–127. (in Chinese)

Yasui, S., and M. Watanabe, 2010: Forcing processes of the summertime circumglobal teleconnection pattern in a dry AGCM. *J. Climate*, **23**, 2093–2114, https://doi.org/10.1175/2009JCLI3323.1.

Yoon, J., and S. Yeh, 2010: Influence of the Pacific decadal oscillation on the relationship between El Niño and the Northeast Asian summer monsoon. *J. Climate*, **23**, 4525–4537, https://doi.org/10.1175/2010JCLI3352.1.

Zhou, F., R. Zhang, and J. Han, 2019: Relationship between the circumglobal teleconnection and Silk Road pattern over Eurasian continent. *Sci. Bull.*, **64**, 374, https://doi.org/10.1016/j.scib.2019.02.014.

Accepted for publication in *Journal of Climate*. DOI 10.1175/JCLI-D-19-0362.1.

653 **Figure Captions**

654 **Figure 1.** (a) Climatological mean of 250-hPa zonal wind and (b) meridional wind in
655 JJA. Counter intervals are 3.0 m s^{-1} in (a) and 1.0 m s^{-1} in (b). Zero contours are
656 omitted. Grey shading in (a) indicates zonal wind is greater than 15.0 m s^{-1}.
657 Color shadings in (b) denote the standard deviation of 250-hPa meridional wind.
658 The bold black lines represent the climatological jet axis during summer. The
659 domain marked by the green rectangle in (b) is used for the latter EOF analyses.

660 **Figure 2.** (a) EOF1, the leading mode of the 250-hPa meridional wind (m s^{-1}) within
661 the domain 55º−70°N, 35º−110°E. Zero contours are omitted. This mode
662 explains 49.3% of the total variance. (b) Time series of the leading mode (PC1;
663 black line) and the HET index (HETI; red line; see text for details).

664 **Figure 3.** The 250-hPa meridional wind anomalies regressed onto the standardized
665 HETI. The contour interval is 0.5 m s^{-1} and the zero contours are not shown. The
666 shading denotes the 95% confidence level based on the Student's *t*-test.

667 **Figure 4.** (a) The vertically integrated (from surface to 100 hPa) baroclinic energy
668 conversion (*CP*) associated with the HET. (b) The vertical integration of the first
669 term ($-\frac{f}{\sigma}v'T'\frac{\partial \bar{u}}{\partial p}$) and (c) the second term ($-\frac{f}{\sigma}u'T'\frac{\partial \bar{v}}{\partial p}$) of *CP*. The contour
670 interval is 0.02 W m^{-2}. Zero contours are not shown. The red box in (a) indicates
671 the wave train domain 45º−75°N, 30°W−150°E.

672 **Figure 5.** The vertical section of baroclinic energy conversion *CP* (Shadings) and its
673 first term ($-\frac{f}{\sigma}v'T'\frac{\partial \bar{u}}{\partial p}$; Contours) along 63°N. The contour interval is 2.0×10^{-5}

Accepted for publication in *Journal of Climate*. DOI 10.1175/JCLI-D-19-0362.1.

674 $m^2\ s^{-3}$, and zero contours are omitted.

675 **Figure 6.** Baroclinic energy conversion *CP* associated with the HET integrated over
676 (a) mid-troposphere (700−300 hPa) and (b) lower troposphere (1000−700 hPa).
677 The contour interval is 0.02 W m^{-2}. Zero contours are not shown.

678 **Figure 7.** The vertical section of (a) the disturbance component ($v'T'$; Units: m K s^{-1})
679 and (b) the basic state component ($-\frac{f}{\sigma}\frac{\partial \bar{u}}{\partial p}$; Units: 1.0×10^{-5} m K^{-1} s^{-2})
680 associated with $-\frac{f}{\sigma}v'T'\frac{\partial \bar{u}}{\partial p}$ along 63°N. The contour intervals in (a) and (b)
681 are 0.5 and 1.0, respectively. Zero contours are omitted in (a).

682 **Figure 8.** The vertical section of meridional wind anomalies (v'; Shadings; Units: m
683 s^{-1}) and temperature anomalies (T'; Black contours) regressed onto the
684 normalized HETI along 63°N. The contour interval is 0.2 K, and zero contours
685 are bolded.

686 **Figure 9.** (a) The vertical section of terms associated with the basic state: (a) $\frac{f}{\sigma}$
687 (Units: Pa K^{-1} s^{-1}), (b) $\frac{R\bar{T}}{C_p p}$ (Units: 1.0×10^{-4} K Pa^{-1}), (c) $\frac{\partial \bar{T}}{\partial p}$ (Units:
688 1.0×10^{-4} K Pa^{-1}), (d) the climatological mean of temperature (Units: K), (e)
689 $-\frac{\partial \bar{u}}{\partial p}$ (Units: 1.0×10^{-4} m Pa^{-1} s^{-1}), and (f) the climatological mean of zonal
690 wind (Units: m s^{-1}), along 63°N. The contour intervals in (a), (b), (d), (e), and (f)
691 are 0.1, 3.0, 5.0, 1.0 and 1.0, respectively. Values greater than 0.3 in (a) are
692 shaded. Shading in (c) indicates values greater than 12.0 and those greater than
693 6.0 in the lower troposphere (1000−700 hPa). The dashed lines in (a)−(d) are

Accepted for publication in *Journal of Climate*. DOI 10.1175/JCLI-D-19-0362.1.

165°W, 95°W, 0°, and 150°E, respectively.

Figure 10. (a) The first term of *CP* ($-\frac{f}{\sigma}v'T'\frac{\partial \bar{u}}{\partial p}$; Units: 1.0×10^{-5} m^2 s^{-3}) and the terms associated with (c, e) disturbance and (b, d, f) basic state: (b) $-\frac{f}{\sigma}\frac{\partial \bar{u}}{\partial p}$ (Units: 1.0×10^{-5} m K^{-1} s^{-2}), (c) $v'T'$ (Units: m K s^{-1}), (d) $-\frac{\partial \bar{u}}{\partial p}$ (Units: 1.0×10^{-4} m Pa^{-1} s^{-1}), (e) v' (Shadings; Units: m s^{-1}) and T' (Black contours; Units: K), and (f) σ (Units: 1.0×10^{-4} K Pa^{-1}), at 400 hPa. The contour intervals in (a), (b), (c), (d), (e), and (f) are 2.0, 2.0, 0.3, 1.0, 0.2, and 0.1, respectively. Zero contours are not shown. The red stars in (a) indicate the positions of the largest positive (at 63°N, 52.5°E) and negative (at 64.5°N, 78°E) value, respectively.

Figure 11. (a) The first term of *CP* ($-\frac{f}{\sigma}v'T'\frac{\partial \bar{u}}{\partial p}$; Units: 1.0×10^{-5} m^2 s^{-3}) and the terms associated with (c, e) disturbance and (b, d, f) basic state: (b) $-\frac{f}{\sigma}\frac{\partial \bar{u}}{\partial p}$ (Units: 1.0×10^{-5} m K^{-1} s^{-2}), (c) $v'T'$ (Units: m K s^{-1}), (d) $-\frac{\partial \bar{u}}{\partial p}$ (Units: 1.0×10^{-4} m Pa^{-1} s^{-1}), (e) v' (Color shadings; Units: m s^{-1}) and T' (Contours; Units: K), and (f) σ (Units: 1.0×10^{-4} K Pa^{-1}), at 925 hPa. The contour intervals in (a), (b), (c), (d), (e), and (f) are 2.0, 2.0, 0.3, 0.5, 0.2 and 0.1, respectively. Zero contours are not shown. The black shading represents mountains higher than 800 m.

Figure 12. The temperature anomalies (T'; Units: K) and meridional wind anomalies

Accepted for publication in *Journal of Climate*. DOI 10.1175/JCLI-D-19-0362.1.

713 (v'; Units: m s^{-1}) regressed onto the normalized HETI along 63°N at (a) 400
714 hPa and (b) 925 hPa. The vertically dashed line in (a) indicate the longitude
715 where v' peaks, and the red stars indicate the corresponding values of v' and
716 T', respectively.
717
718
719
720
721

Accepted for publication in *Journal of Climate*. DOI 10.1175/JCLI-D-19-0362.1.

722 **Table 1.** $-\frac{f}{\sigma}v'T'\frac{\partial \bar{u}}{\partial p}$ (W m^{-2}) averaged over the Northern Hemisphere (NH;

723 5º−85°N) and the wave train domain (WTD; 45º−75°N, 30°W−150°E). The values

724 have been integrated in the mid-troposphere (700−300 hPa) and lower troposphere

725 (1000−700 hPa), respectively.

	NH	WTD
700−300 hPa	0.0023	0.0106
1000−700 hPa	0.0021	0.0100

726

727

Accepted for publication in *Journal of Climate*. DOI 10.1175/JCLI-D-19-0362.1.

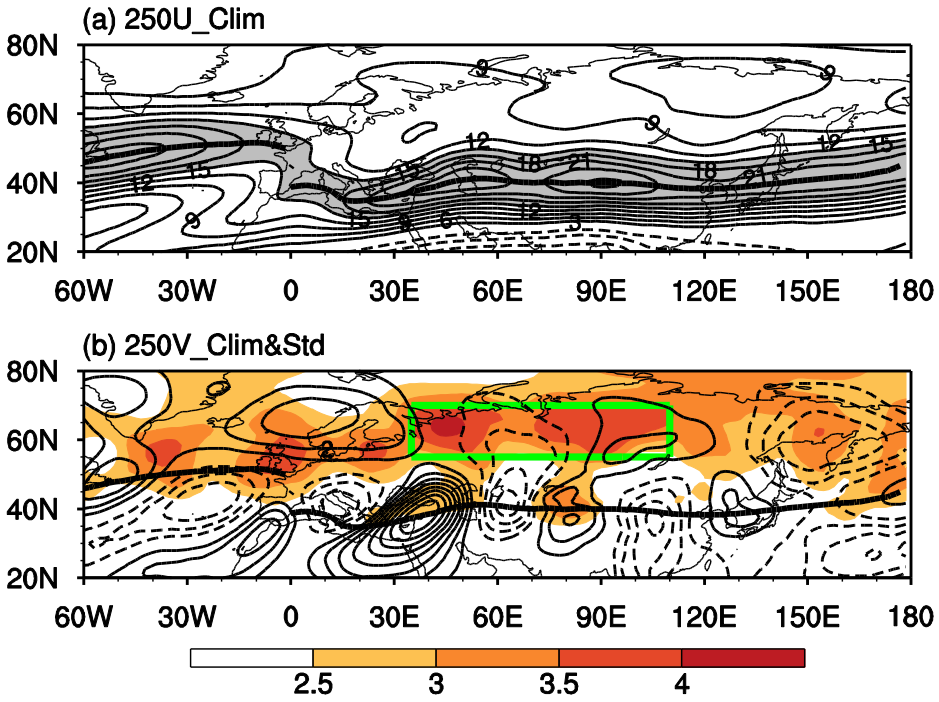

728
729

730 **Figure 1.** (a) Climatological mean of 250-hPa zonal wind and (b) meridional wind in
731 JJA. Counter intervals are 3.0 m s^{-1} in (a) and 1.0 m s^{-1} in (b). Zero contours are
732 omitted. Grey shading in (a) indicates zonal wind is greater than 15.0 m s^{-1}.
733 Color shadings in (b) denote the standard deviation of 250-hPa meridional wind.
734 The bold black lines represent the climatological jet axis during summer. The
735 domain marked by the green rectangle in (b) is used for the latter EOF analyses.

736

Accepted for publication in *Journal of Climate*. DOI 10.1175/JCLI-D-19-0362.1.

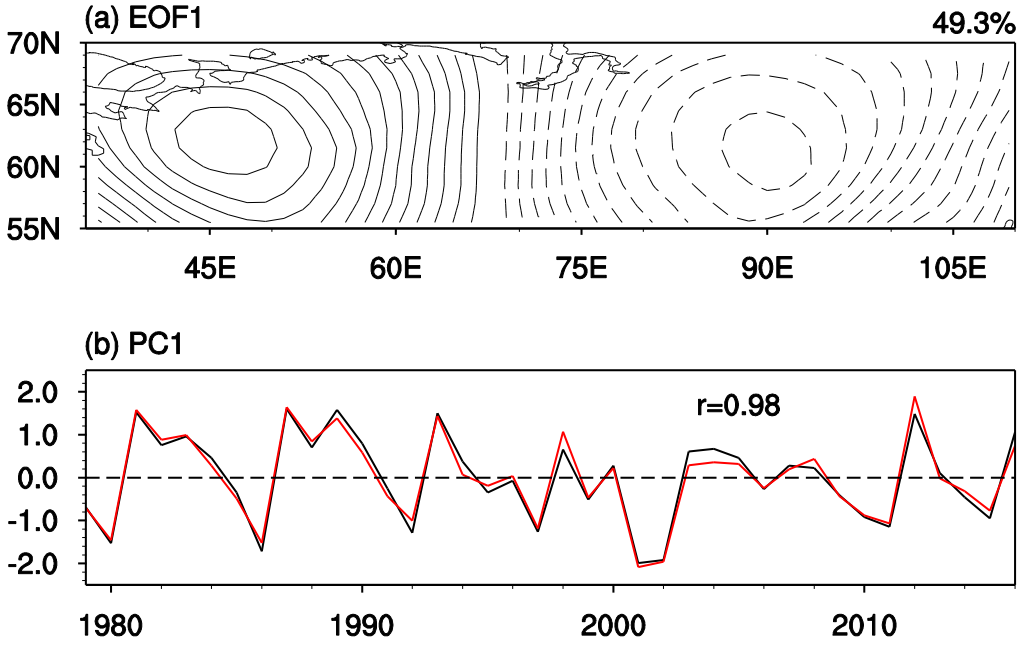

737

738

739 **Figure 2.** (a) EOF1, the leading mode of the 250-hPa meridional wind (m s^{-1}) within

740 the domain 55º−70°N, 35º−110°E. Zero contours are omitted. This mode

741 explains 49.3% of the total variance. (b) Time series of the leading mode (PC1;

742 black line) and the HET index (HETI; red line; see text for details).

743

Accepted for publication in *Journal of Climate*. DOI 10.1175/JCLI-D-19-0362.1.

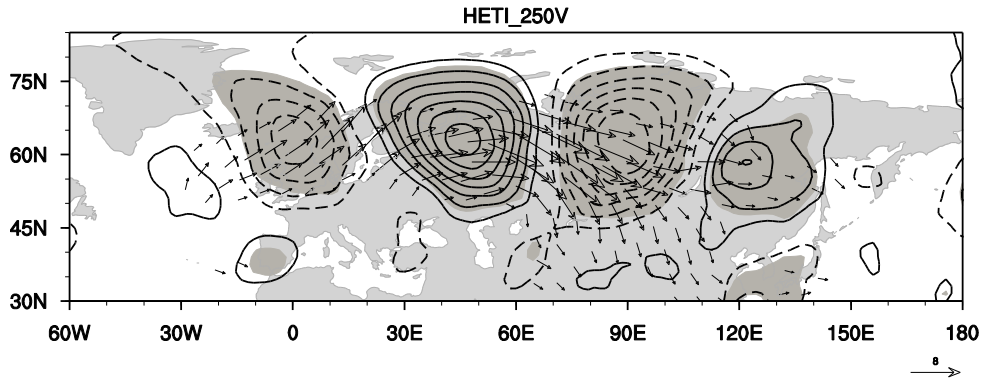

744

745

746 **Figure 3.** The 250-hPa meridional wind anomalies (Contours) regressed onto the
747 standardized HETI and associated horizontal wave activity flux (Vectors). The
748 contour interval is 0.5 m s^{-1} and the zero contours are not shown. The shading
749 denotes the 95% confidence level based on the Student's *t*-test. Vectors less than
750 1.5 m^2 s^{-2} are omitted.

751

Accepted for publication in *Journal of Climate*. DOI 10.1175/JCLI-D-19-0362.1.

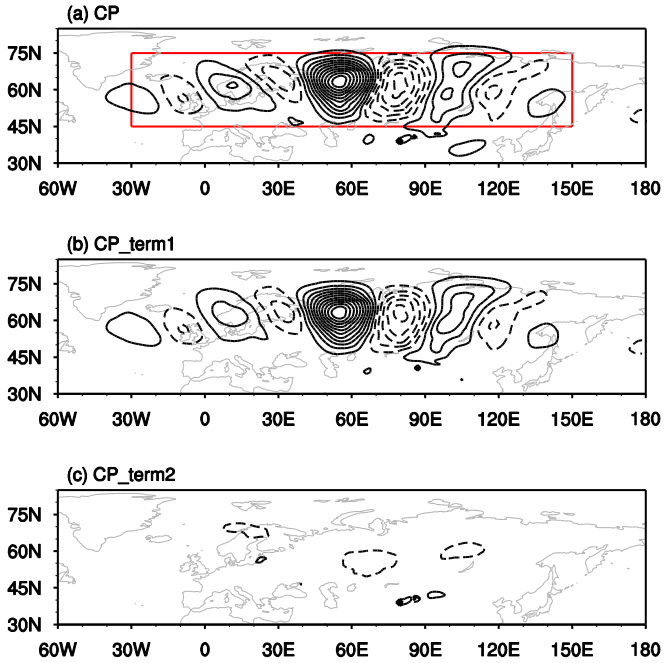

752

753

754 **Figure 4.** (a) The vertically integrated (from surface to 100 hPa) baroclinic energy

755 conversion (*CP*) associated with the HET. (b) The vertical integration of the first

756 term ($-\frac{f}{\sigma}v'T'\frac{\partial \bar{u}}{\partial p}$) and (c) the second term ($\frac{f}{\sigma}u'T'\frac{\partial \bar{v}}{\partial p}$) of *CP*. The contour

757 interval is 0.02 W m^{-2}. Zero contours are not shown. The red box in (a) indicates

758 the wave train domain 45º−75°N, 30°W−150°E.

759

Accepted for publication in *Journal of Climate*. DOI 10.1175/JCLI-D-19-0362.1.

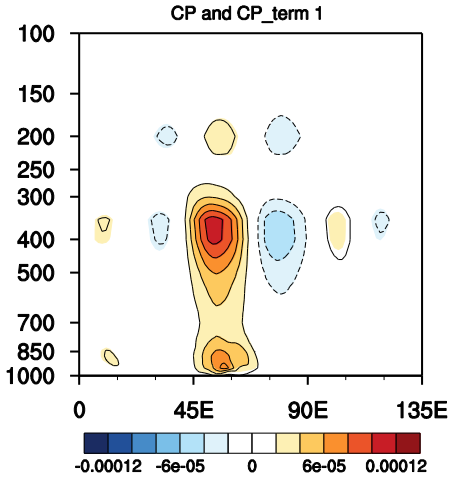

760

761

762 **Figure 5.** The vertical section of baroclinic energy conversion *CP* (Shadings) and its

763 first term ($-\frac{f}{\sigma}v'T'\frac{\partial \bar{u}}{\partial p}$; Contours) along 63°N. The contour interval is 2.0×

764 10^{-5} m^2 s^{-3}, and zero contours are omitted.

765

Accepted for publication in *Journal of Climate*. DOI 10.1175/JCLI-D-19-0362.1.

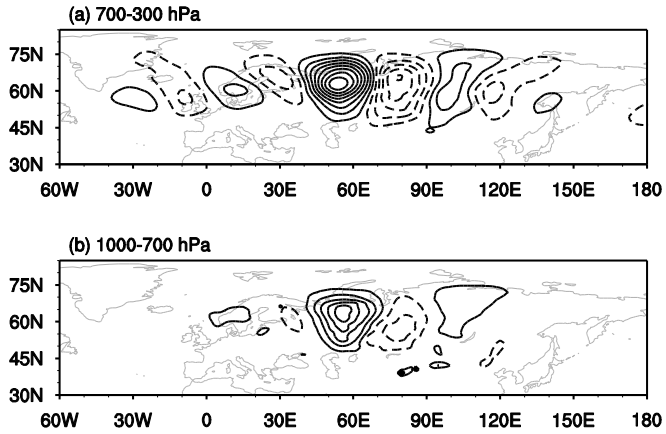

766

767

768 **Figure 6.** Baroclinic energy conversion *CP* associated with the HET integrated over

769 (a) mid-troposphere (700−300 hPa) and (b) lower troposphere (1000−700 hPa).

770 The contour interval is 0.02 W m^{-2}. Zero contours are not shown.

771

772

Accepted for publication in *Journal of Climate*. DOI 10.1175/JCLI-D-19-0362.1.

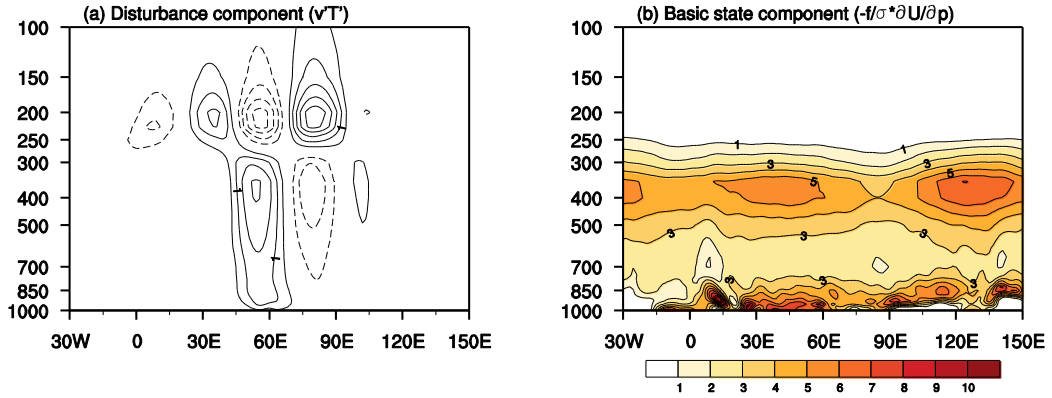

773

774

775

776 **Figure 7.** The vertical section of (a) the disturbance component ($v'T'$; Units: m K s^{-1})

777 and (b) the basic state component ($-\frac{f}{\sigma}\frac{\partial \bar{u}}{\partial p}$; Units: 1.0×10^{-5} m K^{-1} s^{-2})

778 associated with $-\frac{f}{\sigma}v'T'\frac{\partial \bar{u}}{\partial p}$ along 63°N. The contour intervals in (a) and (b)

779 are 0.5 and 1.0, respectively. Zero contours are omitted in (a).

780

781

Accepted for publication in *Journal of Climate*. DOI 10.1175/JCLI-D-19-0362.1.

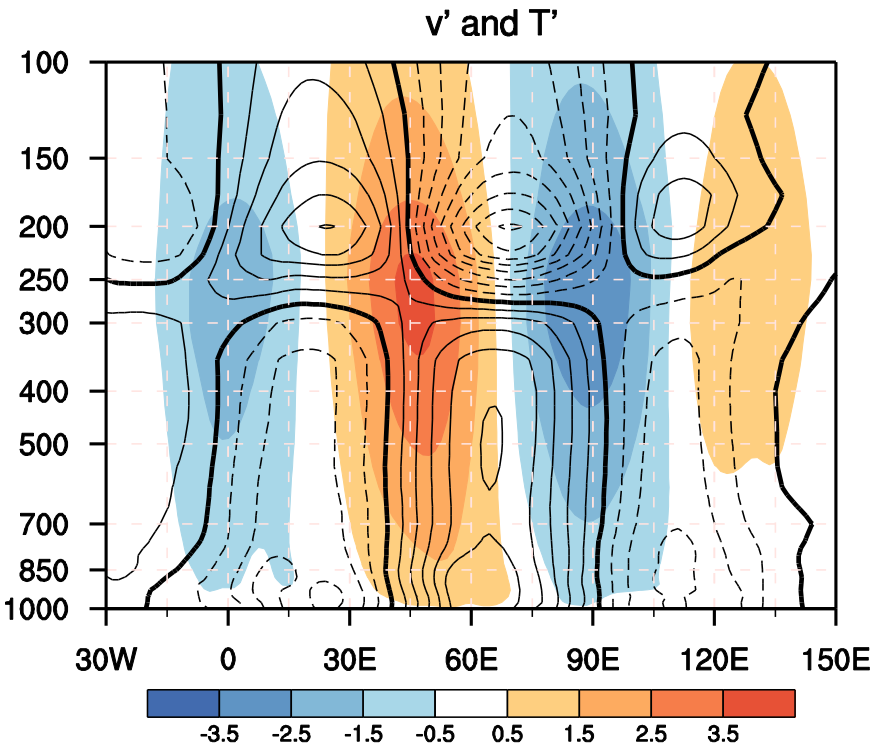

782

783

784 **Figure 8.** The vertical section of meridional wind anomalies (v'; Shadings; Units: m

785 s^{-1}) and temperature anomalies (T'; Black contours) regressed onto the

786 normalized HETI along 63°N. The contour interval is 0.2 K, and zero contours

787 are in bold.

788

789

Accepted for publication in *Journal of Climate*. DOI 10.1175/JCLI-D-19-0362.1.

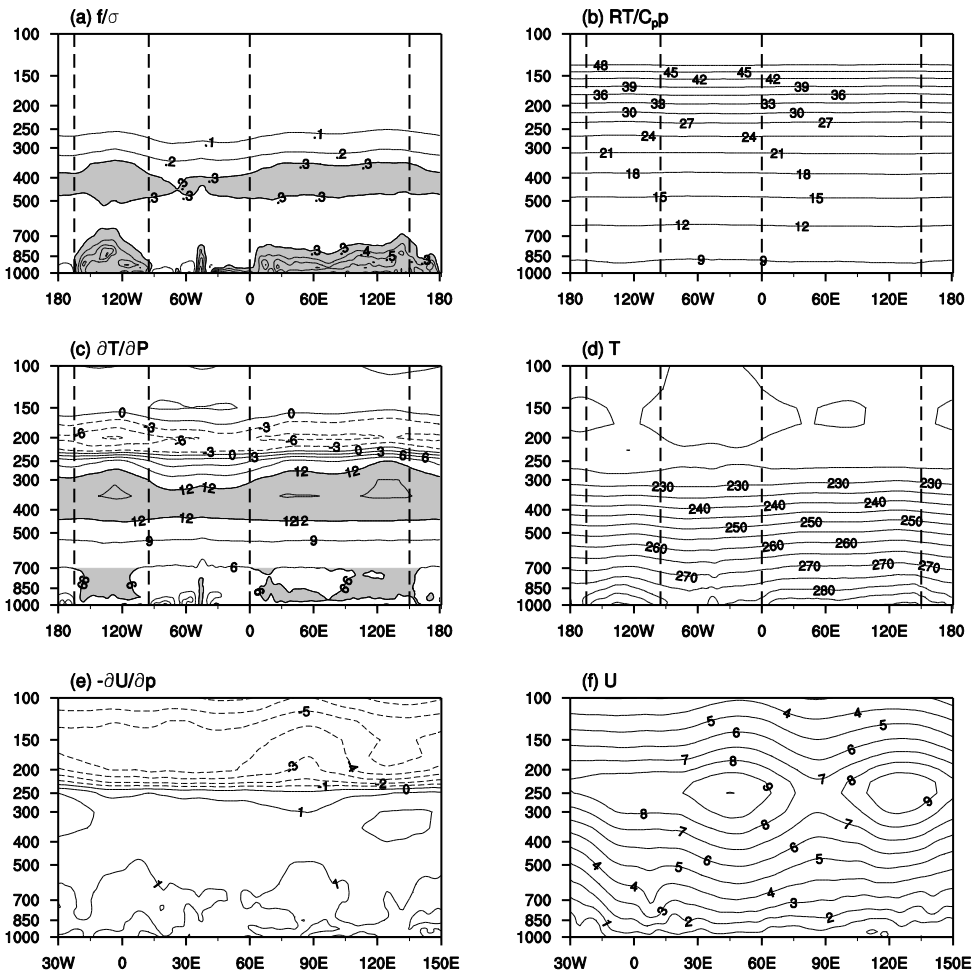

790

791 **Figure 9.** (a) The vertical section of terms associated with the basic state: (a) $\frac{f}{\sigma}$

792 (Units: Pa K^{-1} s^{-1}), (b) $\frac{R\overline{T}}{C_p p}$ (Units: 1.0×10^{-4} K Pa^{-1}), (c) $\frac{\partial\overline{T}}{\partial p}$ (Units: $1.0\times$

793 10^{-4} K Pa^{-1}), (d) the climatological mean of temperature (Units: K), (e) $-\frac{\partial\overline{u}}{\partial p}$

794 (Units: 1.0×10^{-4} m Pa^{-1} s^{-1}), and (f) the climatological mean of zonal wind

795 (Units: m s^{-1}), along 63°N. The contour intervals in (a), (b), (d), (e), and (f) are

796 0.1, 3.0, 5.0, 1.0 and 1.0, respectively. Values greater than 0.3 in (a) are shaded.

797 Shading in (c) indicates values greater than 12.0 and those greater than 6.0 in the

798 lower troposphere (1000−700 hPa). The dashed lines in (a)−(d) are 165°W, 95°W,

799 0°, and 150°E, respectively.

Accepted for publication in *Journal of Climate*. DOI 10.1175/JCLI-D-19-0362.1.

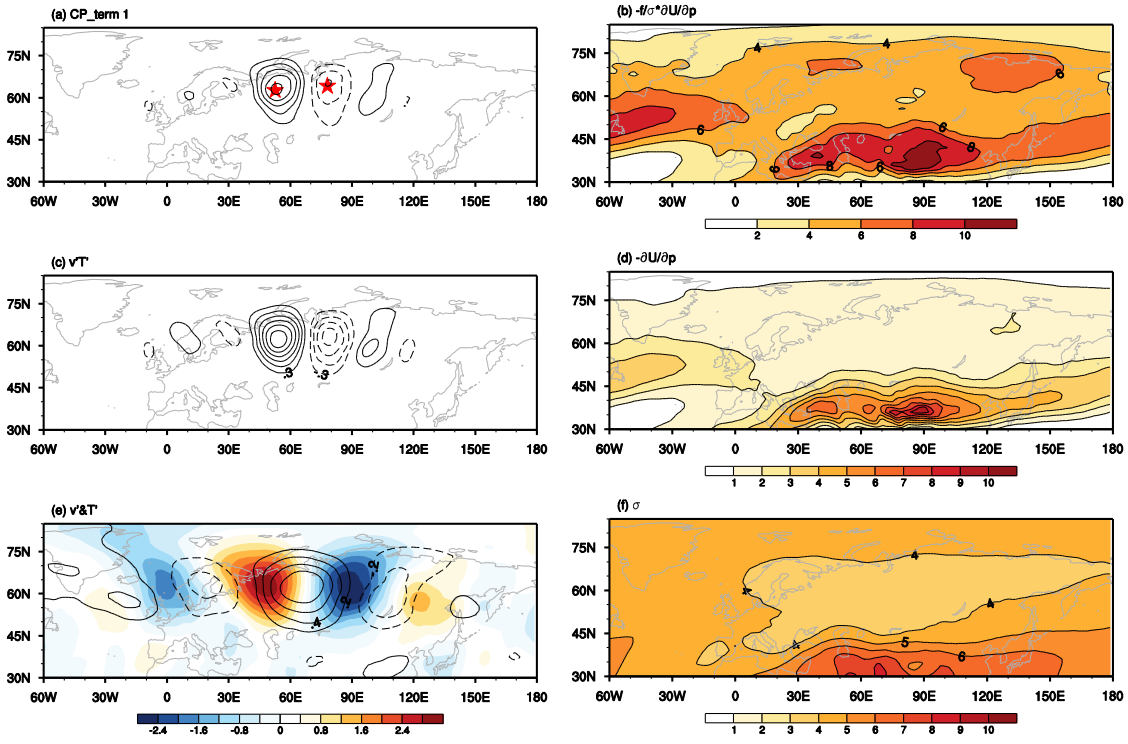

Figure 10. (a) The first term of *CP* ($-\frac{f}{\sigma}v'T'\frac{\partial \bar{u}}{\partial p}$; Units: 1.0×10^{-5} m^2 s^{-3}) and the terms associated with (c, e) disturbance and (b, d, f) basic state: (b) $-\frac{f}{\sigma}\frac{\partial \bar{u}}{\partial p}$ (Units: 1.0×10^{-5} m K^{-1} s^{-2}), (c) $v'T'$ (Units: m K s^{-1}), (d) $-\frac{\partial \bar{u}}{\partial p}$ (Units: 1.0×10^{-4} m Pa^{-1} s^{-1}), (e) v' (Shadings; Units: m s^{-1}) and T' (Black contours; Units: K), and (f) σ (Units: 1.0×10^{-4} K Pa^{-1}), at 400 hPa. The contour intervals in (a), (b), (c), (d), (e), and (f) are 2.0, 2.0, 0.3, 1.0, 0.2, and 0.1, respectively. Zero contours are not shown. The red stars in (a) indicate the positions of the largest positive (at 63°N, 52.5°E) and negative (at 64.5°N, 78°E) value, respectively.

Accepted for publication in *Journal of Climate*. DOI 10.1175/JCLI-D-19-0362.1.

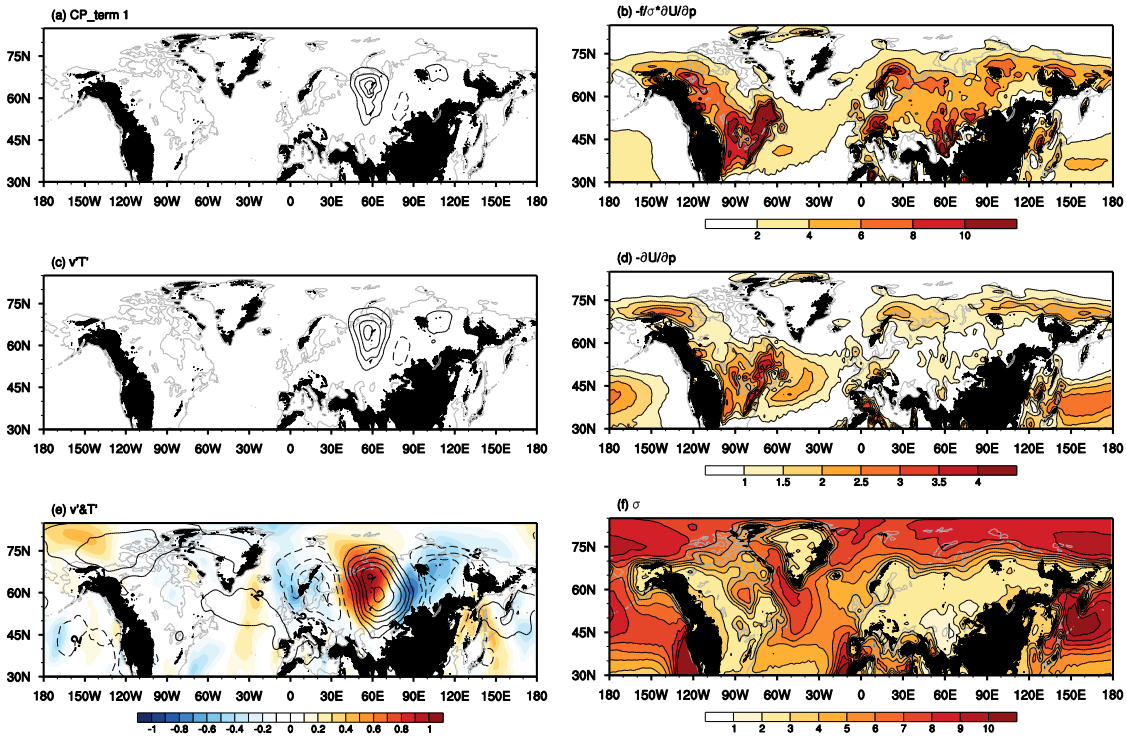

811

812 **Figure 11.** (a) The first term of *CP* ($-\frac{f}{\sigma}v'T'\frac{\partial \bar{u}}{\partial p}$; Units: 1.0×10^{-5} m^2 s^{-3}) and the

813 terms associated with (c, e) disturbance and (b, d, f) basic state: (b) $-\frac{f}{\sigma}\frac{\partial \bar{u}}{\partial p}$

814 (Units: 1.0×10^{-5} m K^{-1} s^{-2}), (c) $v'T'$ (Units: m K s^{-1}), (d) $-\frac{\partial \bar{u}}{\partial p}$ (Units: $1.0\times$

815 10^{-4} m Pa^{-1} s^{-1}), (e) v' (Color shadings; Units: m s^{-1}) and T' (Contours;

816 Units: K), and (f) σ (Units: 1.0×10^{-4} K Pa^{-1}), at 925 hPa. The contour

817 intervals in (a), (b), (c), (d), (e), and (f) are 2.0, 2.0, 0.3, 0.5, 0.2 and 0.1,

818 respectively. Zero contours are not shown. The black shading represents

819 mountains higher than 800 m.

820

821

Accepted for publication in *Journal of Climate*. DOI 10.1175/JCLI-D-19-0362.1.

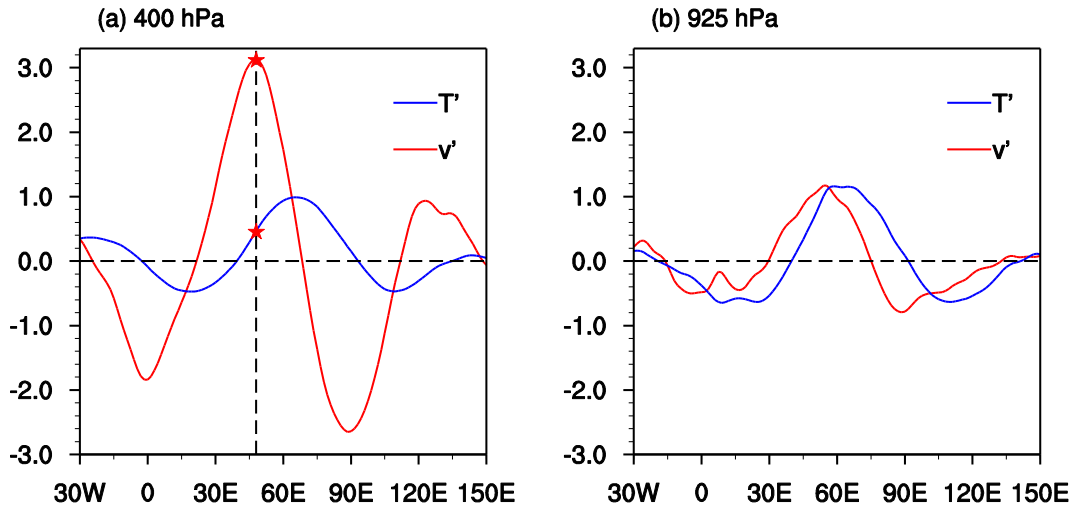

822
823

824 **Figure 12.** The temperature anomalies (T'; Units: K) and meridional wind anomalies
825 (v'; Units: m s^{-1}) regressed onto the normalized HETI along 63°N at (a) 400
826 hPa and (b) 925 hPa. The vertically dashed line in (a) indicate the longitude
827 where v' peaks, and the red stars indicate the corresponding values of v' and
828 T', respectively.

829

830

831

Accepted for publication in *Journal of Climate*. DOI 10.1175/JCLI-D-19-0362.1.